

Chandra X-ray spectroscopy of the very early O supergiant HD 93129A: constraints on wind shocks and the mass-loss rate

David H. Cohen,^{1*} Marc Gagné,² Maurice A. Leutenegger,^{3,4} James P. MacArthur,¹ Emma E. Wollman,^{1,5} Jon O. Sundqvist,⁶ Alex W. Fullerton,⁷ Stanley P. Owocki⁶

¹*Swarthmore College, Department of Physics and Astronomy, Swarthmore, Pennsylvania 19081, USA*

²*West Chester University, Department of Geology and Astronomy, West Chester, Pennsylvania 19383, USA*

³*NASA/Goddard Space Flight Center, Code 662, Greenbelt, Maryland 20771, USA*

⁴*CRESST and University of Maryland, Baltimore County, MD 21250, USA*

⁵*Caltech, Department of Physics, 1200 East California Blvd., Pasadena, California 91125, USA*

⁶*University of Delaware, Bartol Research Institute, Newark, Delaware 19716, USA*

⁷*Space Telescope Science Institute, 3700 San Martin Dr., Baltimore, Maryland 21218, USA*

15 June 2018

ABSTRACT

We present analysis of both the resolved X-ray emission line profiles and the broadband X-ray spectrum of the O2 If* star HD 93129A, measured with the *Chandra* HETGS. This star is among the earliest and most massive stars in the Galaxy, and provides a test of the embedded wind shock scenario in a very dense and powerful wind. A major new result is that continuum absorption by the dense wind is the primary cause of the hardness of the observed X-ray spectrum, while intrinsically hard emission from colliding wind shocks contributes less than 10% of the X-ray flux. We find results consistent with the predictions of numerical simulations of the line-driving instability, including line broadening indicating an onset radius of X-ray emission of several tenths R_* . Helium-like forbidden-to-intercombination line ratios are consistent with this onset radius, and inconsistent with being formed in a wind-collision interface with the star's closest visual companion at a distance of 100 AU. The broadband X-ray spectrum is fit with a dominant emission temperature of just $kT = 0.6$ keV along with significant wind absorption. The broadband wind absorption and the line profiles provide two independent measurements of the wind mass-loss rate: $\dot{M} = 5.2^{+1.8}_{-1.5} \times 10^{-6} M_{\odot} \text{ yr}^{-1}$ and $\dot{M} = 6.8^{+2.8}_{-2.2} \times 10^{-6} M_{\odot} \text{ yr}^{-1}$, respectively. This is the first consistent modeling of the X-ray line profile shapes and broadband X-ray spectral energy distribution in a massive star, and represents a reduction of a factor of 3 to 4 compared to the standard $H\alpha$ mass-loss rate that assumes a smooth wind.

Key words: stars: early-type – stars: mass-loss – stars: winds, outflows – stars: individual: HD 93129A – X-rays: stars

1 INTRODUCTION

With a spectral type of O2 If* (Walborn et al. 2002), HD 93129A is among the earliest, hottest, most massive and luminous O stars in the Galaxy. As such, it has an extremely powerful wind, with a terminal velocity in excess of 3000 km s^{-1} , and a mass-loss rate thought to be in excess of $10^{-5} M_{\odot} \text{ yr}^{-1}$ (Repolust et al. 2004). In fact,

HD 93129A has been considered to have the highest mass-loss rate of any O star in the Galaxy (Taresch et al. 1997; Benaglia & Koribalski 2004). This star, therefore, provides an interesting test of the wind-shock paradigm of massive star X-ray emission, both because of the tremendous kinetic power in its wind and because of the dominant role played by X-ray absorption in such a dense wind. In order to study the X-ray emission and absorption we have analyzed the *Chandra* HETGS spectrum with a focus on individual line profiles. In addition, we analyze the low-resolution, zeroth-

* E-mail: cohen@astro.swarthmore.edu

order ACIS CCD spectrum in order to determine the relative contributions of high-temperature thermal emission and wind attenuation to the observed spectral hardness. These complementary analysis techniques provide information about the temperature and kinematics of the X-ray emitting plasma, about its spatial distribution, and about the wind mass-loss rate.

X-ray emission from O stars is attributed to three mechanisms: (1) Embedded Wind Shocks (EWS), generally assumed to be associated with the Line-Driving Instability (LDI) (Lucy & White 1980; Owocki et al. 1988; Feldmeier et al. 1997; Kahn et al. 2001); (2) Colliding Wind Shocks (CWS) in some binary systems (Stevens et al. 1992; Antokhin et al. 2004; Pittard & Parkin 2010); and (3) Magnetically Confined Wind Shocks (MCWS) for stars with significant dipole magnetic fields (Babel & Montmerle 1997; ud-Doula & Owocki 2002; Gagné et al. 2005). Of these, the EWS mechanism is assumed to operate in all O stars, while CWS may dominate in massive binaries with strong enough winds and MCWS in those small number of O stars with strong, large-scale magnetic fields. The EWS mechanism produces plasma of several million degrees and is associated with relatively soft X-ray emission, while the other two mechanisms produce stronger shocks, higher temperatures, and harder X-ray emission. However, it should be kept in mind that soft X-ray absorption by the bulk wind can harden the observed X-rays from EWS in O stars with high mass-loss rates (Leutenegger et al. 2010).

In high-resolution X-ray spectra, the hallmark of embedded wind shocks is broad emission lines (Kahn et al. 2001; Cassinelli et al. 2001). By analyzing the widths and profile shapes of individual X-ray emission lines in the grating spectra of O stars, the kinematics of the hot, X-ray emitting plasma embedded in the warm, partially ionized bulk wind can be determined, testing the predictions of the EWS scenario. Furthermore, due to preferential absorption of red-shifted line photons from the far hemisphere of O star winds, X-ray emission lines from embedded wind shocks have a characteristic blue-shifted and skewed shape, in proportion to the characteristic wind optical depth (Owocki & Cohen 2001). It recently has been shown that a wind mass-loss rate can be determined by fitting the ensemble of derived characteristic optical depths, given a model of the bulk wind X-ray opacity (Cohen et al. 2010). The initial application of this technique to ζ Pup (O4 If) provided a mass-loss rate determination that was roughly a factor of three lower than the traditional value derived from the strength of the $H\alpha$ emission under the assumption of a smooth, unclumped wind. This lower value is consistent with other recent reassessments (Puls et al. 2006) that do account for small-scale wind clumping, which affects density-squared diagnostics such as $H\alpha$ emission strength. The associated clumping factors are consistent with those seen in numerical simulations of the LDI (Runacres & Owocki 2002; Dessart & Owocki 2005). Indeed, there is a consensus emerging that many, if not all, O stars' mass-loss rates must be lowered by factors of several due to the effects of clumping (Hamann et al. 2008). In this context, the X-ray line profile mass-loss rate diagnostic is especially useful, as it is not affected by small-scale clumping, as long as the individual clumps are optically thin to X-rays (Cohen et al. 2010).

Both numerical simulations and the lack of significant

observed X-ray variability indicate that clumps in O star winds are on quite small scales, with sizes $\ell \ll R_*$. Since even the entire wind of HD 93129A is only marginally optically thick to bound-free absorption of X-rays, it is very likely that such small clumps will be individually quite optically thin to X-rays. This means they cannot have much of the self-shadowing that would reduce the exposure of wind material to X-rays, and would thus lead to a significant “porosity” reduction in the overall absorption. An important point here then is that, while such porosity requires a strong clumping (with individual clumps that are optically thick), a clumped wind need not be porous (if the clumps are optically thin).¹

HD 93129A lies in the Trumpler 14 cluster in the Carina nebula, at a distance of 2.3 kpc, but with a modest visual extinction of $A_V = 2.3$ (Townsend et al. 2011; Gagné et al. 2011). It has a visual companion, HD 93129B, at a separation of $2.7''$, with a spectral type of O3.5, and it also has a closer visual companion (HD 93129Ab) detected using the HST Fine Guidance Sensor (FGS) at a separation of $0.053''$ (Nelán et al. 2004, 2010). This closer companion is also estimated to have a spectral type of O3.5. Non-thermal radio emission has been detected from the system, presumably indicating the existence of colliding wind shocks (Benaglia et al. 2006). This motivated the initial CWS interpretation of low-resolution *Chandra* CCD spectral measurements of the relatively hard X-rays from HD 93129A (Evans et al. 2003), although given the large separation of components Aa and Ab (over 100 AU \approx 1000 R_*), any X-ray emission associated with the wind interaction zone should be relatively weak and the overall emission is likely dominated by EWS emission arising much closer to the photosphere of component Aa. Gagné et al. (2011) has recently suggested that only 10 to 15 percent of the X-ray emission is due to CWS X-rays. Furthermore, given the high wind mass-loss rate of HD 93129A, significant attenuation of the soft X-ray emission is expected. This paper represents an attempt to account for wind absorption when analyzing the star's X-ray properties.

Detailed analysis and modeling of the optical and UV spectra of HD 93129A was presented by Taresch et al. (1997). That work included an analysis of the interstellar absorption features in the UV, which yielded a hydrogen column density measurement of $N_H = 2.5 \times 10^{21} \text{ cm}^{-2}$ that is basically consistent with the observed reddening and inferred extinction ($N_H = 3.7 \times 10^{21} \text{ cm}^{-2}$ is implied by the color excess). Important results from the UV and optical spectral analysis include a very high wind mass-loss rate and terminal velocity in addition to a bolometric luminosity in excess of $2 \times 10^6 L_\odot$ and evidence for non-solar abundances in line with CNO processing (a nitrogen abundance several times solar and carbon and oxygen abundances a

¹ In this paper we refer to “optically thin clumping” when discussing clumps that do not have a porosity effect but do have an effect on $H\alpha$, reserving “porosity” to describe the effects of optically thick clumps. For the unmodified term “clumping”, the reader should bear in mind that density-squared diagnostics such as $H\alpha$ will still always be affected, but that X-ray transmission will be affected by an associated porosity if and only if the clumps are optically thick. Finally, we note that a given clump or clump distribution may be optically thin at one wavelength and thick at others.

Table 1. Stellar and wind parameters adopted from Taresch et al. (1997) and Repolust et al. (2004) (in parentheses).

parameter	value
Mass	(95 M_{\odot})
T_{eff}	52000 K (42500 K)
R_*	19.7 R_{\odot} (22.5 R_{\odot})
$\log L_*$	6.4 L_{\odot} (6.17 L_{\odot})
$v_{\text{rot}} \sin i$	(130 km s^{-1})
v_{∞}	3200 km s^{-1} (3200 km s^{-1})
β	0.7 (0.8)
\dot{M}	$1.8 \times 10^{-5} M_{\odot} \text{ yr}^{-1}$ ($2.6 \times 10^{-5} M_{\odot} \text{ yr}^{-1}$)

factor of a few lower than solar). These authors estimate a zero-age main sequence mass of 120 M_{\odot} for HD 93129A. More recent analysis by Repolust et al. (2004) finds a significantly lower effective temperature and a modestly lower bolometric luminosity along with a higher wind mass-loss rate. The stellar parameters derived from these two studies are summarized in Table 1. We note that the presence of the close binary companion will affect the radius determination, and related quantities. Given that the companion is about a magnitude dimmer than the primary, this effect will be small (Repolust et al. 2004).

We describe the *Chandra* HETGS data in §2. In §3 we analyze the line profiles seen in the grating spectrum and also fit global thermal emission models to the low-resolution but higher signal-to-noise zeroth order spectrum. We discuss the implications of these analyses for the three mechanisms of O star X-ray emission in §4, and summarize our conclusions in §5.

2 THE *Chandra* DATA

The data we use in this paper were taken between 8 November 2005 and 5 December 2005 in seven separate pointings, with a total effective exposure time of 137.7 ks. All observations employed the Advanced CCD Imaging Spectrometer with the High Energy Transmission Grating Spectrometer (ACIS-S/HETGS) (Canizares et al. 2005), providing dispersed spectra in the MEG and HEG grating arrays, as well as a low-resolution CCD spectrum from the zeroth-order image. The grating data have been presented previously in Westbrook et al. (2008) and Walborn (2008), and in Nichols et al. (2011).

The field is crowded with X-ray sources, but only HD 93129B, our target’s visual companion, is bright enough and close enough to HD 93129A to pose a potential problem in the data extraction. In Fig. 1 we show the center of the ACIS detector for the longest of the seven separate exposures, with the MEG and HEG extraction regions indicated, and the zeroth-order images of components A and B labeled. The CCDs that compose the ACIS detector have modest intrinsic energy resolution (of roughly $E/\Delta E = 20$ to 50), allowing us to assess the spectral energy distribution of each source as indicated by the color coding in the figure. For this particular exposure, component B, which is 2.7'' southeast of component A, lies in the MEG and HEG extraction regions,

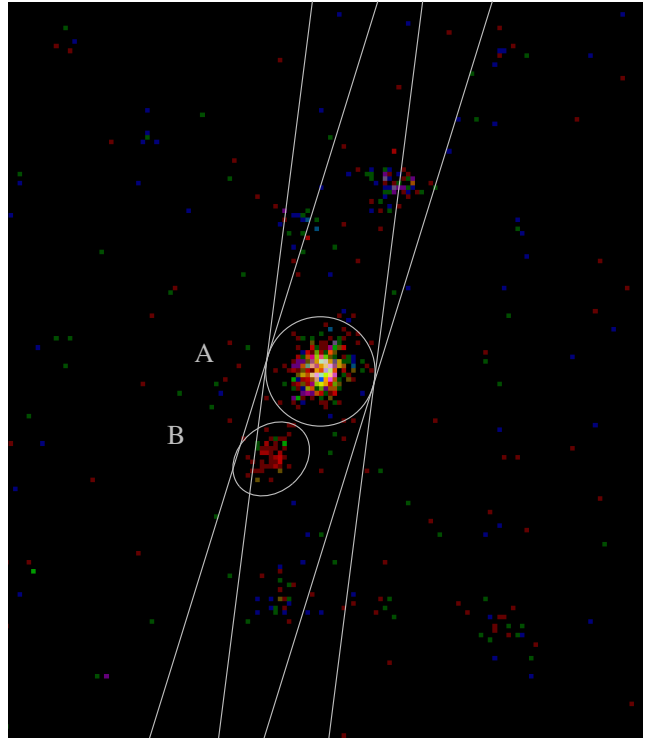


Figure 1. The central region of the ACIS detector from the longest single exposure (Obs ID 7204; exposure time of 34 ks, corresponding to 25 percent of the total exposure time), showing the zeroth order image of HD 93129A (indicated by the circle), along with several other sources. HD 93129B is labeled and located 2.7'' to the southeast of component A (and indicated by the modestly elongated ellipse). The detected photons are color coded according to energy, with low energies (0.5 to 1.5 keV) red, medium energies (1.5 to 2.5 keV) green, and high energies (2.5 to 8 keV) blue. Component B is clearly separable from component A and is softer and weaker (by roughly a factor of ten) than component A. Its relative weakness and softness are quantified in Fig. 2. The negative and positive MEG and HEG grating arm extraction regions are outlined in white (HEG is more vertical, MEG is angled to the upper right and lower left). Note that these have a somewhat different orientation in each observation. The zeroth order image of component B lies mostly within both of these extraction regions, indicating possible contamination of the dispersed spectra of HD 93129A.

and therefore is a potential source of contamination of the dispersed spectra of component A.

Due to the varying roll angle of the *Chandra* instrument, component B does not lie fully in the extraction regions of component A for all of the seven separate observations. Furthermore, as shown in Fig. 2, its photon flux is an order of magnitude lower than that of component A. Finally, the spectral energy distribution of component B is much softer than that of component A (this can also be seen, qualitatively, in the color coding of Fig. 1). In fact, there are almost no counts from component B at energies greater than 1.2 keV, corresponding to a wavelength of 10 Å. Thus, the dispersed spectra of component A are unaffected by contamination from component B below this wavelength. At wavelengths above 10 Å, however, there is likely to be modest contamination. We note that the 2.7'' offset corresponds

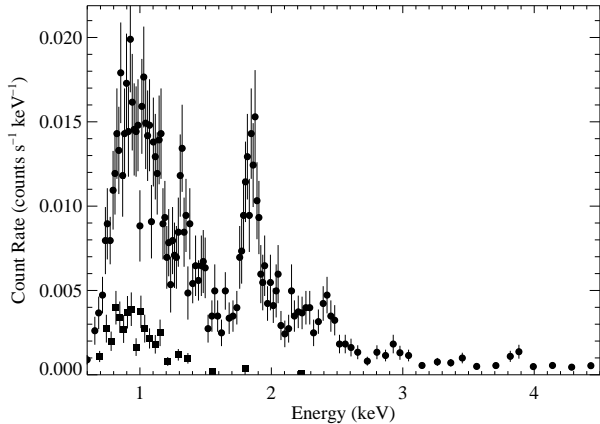


Figure 2. The extracted ACIS CCD spectra – zeroth order – from the seven coadded pointings (circles) and the same for HD 93129B (squares). Note that above 1.2 keV (below 10 Å), the contamination of the grating spectra of component A by that of component B should be negligible.

to a relative shift in the dispersed MEG spectrum of roughly 1500 km s^{-1} , which could artificially broaden the emission lines of component A. We therefore restrict the analysis of the grating spectra in this paper to wavelengths shortward of 10 Å.

We note also that the close binary companion Ab detected at $0.05''$ with the FGS is completely unresolved by *Chandra* so the spectra we analyze in this paper are a composite of the two components. However, the spectral type of Ab is tentatively identified as being the same as that of component B (O3.5 V) (Nelán et al. 2004), so the composite spectrum, especially below 10 Å, is likely dominated by component Aa. We discuss the colliding wind X-ray emission due to this close visual companion in §3.3.

After centroiding the zeroth-order image of component A in each of the seven separate observations, we coadded the observations and extracted the first-order MEG and HEG spectra, as well as the zeroth-order ACIS CCD spectrum shown in Fig. 2. The coadded negative and positive first-order spectra (both MEG and HEG) are shown in Fig. 3. The MEG spectrum has a FWHM resolution of 2.3 mÅ and the HEG, with a lower sensitivity, has a resolution of 1.2 mÅ . In the 5 to 10 Å region where most of the counts are, these correspond to resolving powers of roughly $\lambda/\Delta\lambda = 300$ to 600 in the MEG.

Even with the coaddition of seven separate pointings, for an effective exposure time of 137.7 ks, the spectra have quite low signal-to-noise. This is due both to the great distance to HD 93129 (2.3 kpc) and also to the large interstellar column density, which causes significant attenuation of the soft X-ray emission from the star. As we will show in §3, there is also significant X-ray attenuation from the dense stellar wind. The appearance of the *Chandra* grating spectra of HD 93129A is certainly significantly harder than that of other normal O stars, but this is due primarily to attenuation and not to high temperatures, as can be seen qualitatively in Fig. 3 from the dominance of the He-like lines (Si XIII, Mg XI) over the corresponding H-like lines (Si XIV,

Mg XII), especially for silicon. This qualitative impression is borne out by quantitative modeling presented in §3.3.

Only a handful of lines are present in the MEG spectrum (and even fewer in the lower signal-to-noise HEG spectrum). The small number of visible lines is affected by the overall low signal-to-noise and the aforementioned attenuation, which renders the normally quite strong Fe XVII and O lines longward of 15 Å completely absent. And it is exacerbated by the very large line widths, which spread the modest number of line photons over many pixels. After discarding the very weak lines longward of 10 Å due to contamination from component B, we are left with five lines and blended line complexes detected with greater than 3σ significance: the He-like S XV complex near 5.1 Å, the Ly α line of Si XIV at 6.18 Å, the He-like Si XIII complex near 6.7 Å, the Mg XII Ly α line at 8.42 Å, and the He-like Mg XI complex near 9.2 Å. The weak Mg XI He β line at 7.85 Å is not detected above the 3σ threshold. Not shown in the figure are very weak Ne IX and Ne X lines between 12 Å and 14 Å, which are affected by contamination by the softer X-ray emission from component B, as discussed above.

3 SPECTRAL ANALYSIS

3.1 Resolved emission lines

By fitting a simple, empirical line profile model (Owocki & Cohen 2001) to the Doppler-broadened emission lines, we can simultaneously determine the kinematics of the X-ray emitting plasma and the degree of attenuation by the wind in which the hot, shock-heated plasma is embedded. The specific parameters of the Owocki & Cohen (2001) model are the onset radius of the X-ray emission (R_o) and the fiducial optical depth of the bulk wind, $\tau_* \equiv \kappa \dot{M}/4\pi R_* v_\infty$. Note that τ_* is expected to vary from line to line due to the wavelength dependence of the wind opacity, κ .

The fitted R_o values derived from the data are expected to be several tenths of a stellar radius above the photosphere, based on simulations of the line-driving instability (LDI) (Owocki et al. 1988; Feldmeier et al. 1997; Runacres & Owocki 2002). By deriving values for this parameter from the individual lines in the *Chandra* spectrum of HD 93129A, we can test the LDI scenario for embedded wind shocks in the most extreme O star wind. And the values we derive for the fiducial optical depth, τ_* , can be used to derive a mass-loss rate by fitting the ensemble of values, given a model of the wind opacity, as has been shown by Cohen et al. (2010).

Following the procedure described in Cohen et al. (2010), we assess the continuum level near each line by fitting a small region of the spectrum on either side of the line, and then fit a profile model plus the continuum model (with the level fixed at the value found from fitting the nearby continuum). We allow the normalization, R_o , and τ_* , to be free parameters of the fit, while fixing the velocity law parameter at $\beta = 0.7$ (Taresch et al. 1997) and the terminal velocity at the value determined from the analysis of UV observations, $v_\infty = 3200 \text{ km s}^{-1}$ (Taresch et al. 1997; Repolust et al. 2004). We find the best-fit model parameters by minimizing the C statistic (Cash 1979), and assign confidence limits individually to each model parameter

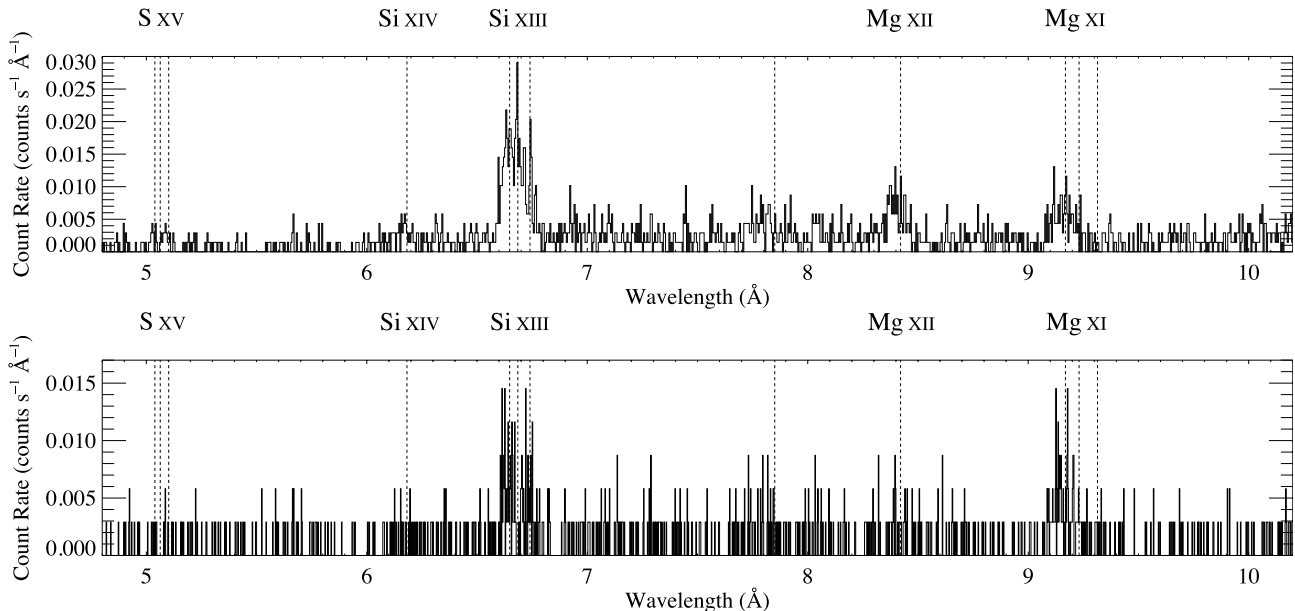


Figure 3. The extracted MEG (top) and HEG (bottom) spectra from the seven coadded pointings. Note the different y-axis scales on the two figures. The wavelengths of lines expected to be present in normal O star *Chandra* spectra are indicated by the vertical dotted lines.

(while allowing the other free parameters to vary) according to the formalism in Press et al. (2007). We fit the MEG and HEG data simultaneously. We perform all of this modeling and data analysis in XSPEC v.12.6, using the custom model *windprofile*².

For the helium-like complexes, which effectively comprise three blended lines each (resonance (r), intercombination (i), and forbidden (f)), we fit three profile models simultaneously (using the custom model *hewind*), with the R_o and τ_* parameters tied together for each of the three lines, as described in Leutenegger et al. (2006). The overall normalization and the $\mathcal{G} \equiv (f+i)/r$ ratio are explicit fit parameters, while the diagnostically important $\mathcal{R} \equiv f/i$ ratio is a function of radius, via the radial dependence of the photoexcitation rate of electrons out of the upper level of the forbidden line into the upper level of the intercombination line. This physics is controlled in our modeling by the same R_o parameter that describes the onset radius of X-ray emission. Lower values of R_o give more plasma close to the photosphere, where it is more strongly affected by photoexcitation, providing a lower $\mathcal{R} \equiv f/i$ value than if R_o were larger and the overall photoexcitation rate were lower. Thus, R_o controls both the line widths and the relative strengths of the intercombination and forbidden lines in the observed spectrum in a self-consistent manner. For the photoexcitation modeling, we use UV fluxes from a TLUSTY $T_{\text{eff}} = 42500$ K, $\log g = 3.75$ model atmosphere (Lanz & Hubeny 2003), and the atomic parameters from Dere et al. (2007).

The number of free parameters in the models – both for the single lines and for the He-like complexes – is kept to

a minimum. We fix the wind terminal velocity ($v_\infty = 3200$ km s⁻¹) and the velocity law parameter ($\beta = 0.7$) at the value determined from the UV data. There is an extensive discussion of the sensitivity of the important model parameters, τ_* and R_o , to these, and other, fixed parameters as well as the effect of such factors as background subtraction and continuum placement in §4.3 of Cohen et al. (2010), to which we refer the reader.

The results of our wind profile fits to the five lines and line complexes are shown in Fig. 4 for the single Ly α lines and Fig. 5 for the three He-like line complexes. The quantitative results are summarized in Tab. 2. We note that when we increase the wind velocity parameter, β , from 0.7 to 1.0, the characteristic optical depth values, τ_* , increase by roughly 30%, while the onset radii, R_o , increase by several tenths of a stellar radius. Similarly, there is sensitivity of the important derived parameters to the assumed wind terminal velocity. For a higher terminal velocity of 3400 km s⁻¹, the best-fit τ_* values decrease by roughly 20% and increase by the same amount when we use a lower terminal velocity of 3000 km s⁻¹. The onset radii, R_o , vary by roughly 10% for these changes in terminal velocity. We note that these systematic uncertainties – especially for τ_* – are small compared to the statistical errors.

Before we move on to interpreting these model-fitting results, we report on a few experiments involving fitting different types of models to these same emission lines. Specifically, Gaussian profiles have traditionally been fit to the broadened emission lines seen in O stars. Therefore, we fit the highest signal-to-noise single line in the spectrum, the Mg XII Ly α line, with an unshifted Gaussian. As expected from the asymmetry seen in the bottom panel of Fig. 4, the fit is poor (the wind profile fit is preferred at > 99.99%). Allowing the Gaussian centroid to be a free parameter, we find an improved fit with a large centroid blue shift (to $\lambda = 8.401$ Å), equivalent to -730 ± 200 km s⁻¹, and a

² The *windprofile* model's implementation in XSPEC is described at heasarc.gsfc.nasa.gov/docs/xanadu/xspec/models/windprof.html, as is the *hewind* model we use to fit helium-like complexes.

Table 2. Wind profile model fit results

ion	wavelength ^a (Å)	τ_*	R_o (R_*)	normalization ^b (10^{-6} ph cm ⁻² s ⁻¹)
S XV	5.0387, 5.0648, 5.1015	$0.32^{+1.36}_{-0.32}$	$1.16^{+0.44}_{-0.15}$	$4.11^{+1.14}_{-1.11}$
Si XIV	6.1822	$1.64^{+1.30}_{-1.26}$	$1.01^{+0.32}_{-0.01}$	$1.48^{+0.49}_{-0.41}$
Si XIII	6.6479, 6.6866, 6.7403	$0.81^{+0.63}_{-0.39}$	$1.37^{+0.12}_{-0.14}$	$16.8^{+1.1}_{-0.8}$
Mg XII	8.4210	$1.03^{+1.12}_{-0.59}$	$1.44^{+0.27}_{-0.27}$	$4.00^{+0.64}_{-0.47}$
Mg XI	9.1687, 9.2297, 9.3143	$2.84^{+0.72}_{-1.59}$	$1.20^{+0.88}_{-0.19}$	$16.1^{+1.1}_{-1.4}$

^a Closely spaced doublets in the Ly α lines and He-like intercombination lines are fit with a single profile model centered at the emissivity-weighted wavelength of the two components.

^b For the He-like complexes, the total normalization of all the lines in the complex is indicated.

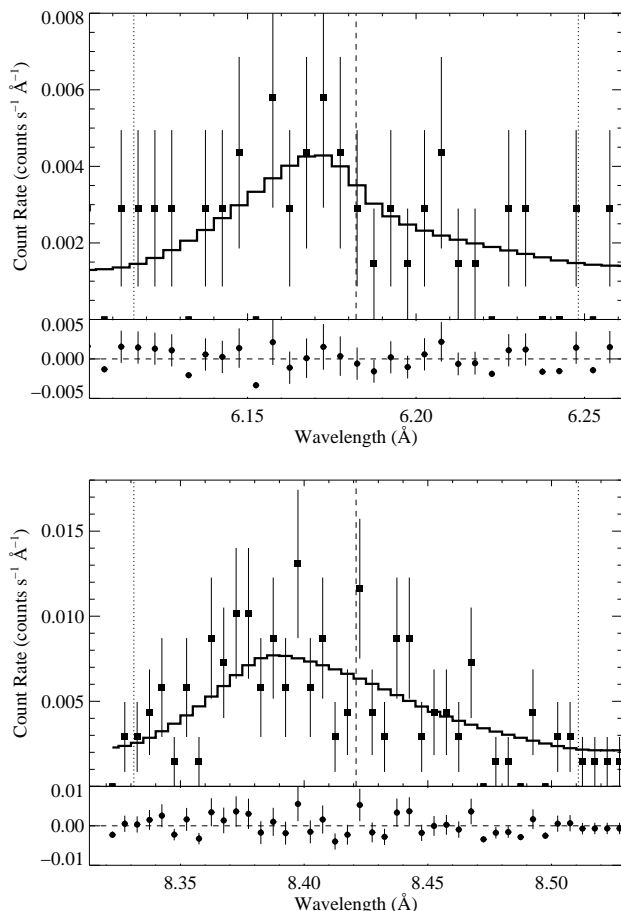


Figure 4. The MEG data for both individual lines with sufficient signal-to-noise to warrant profile fitting, along with the best-fit profile model for each line (histogram). These are the Ly α lines of Si XIV, at 6.18 Å (top), and Mg XII, at 8.42 Å (bottom). The laboratory rest wavelength of each line is indicated by a vertical dashed line and the Doppler shifts associated with the (positive and negative) terminal velocity are indicated by the vertical dotted lines. Poisson error bars are indicated on each data point. Note that the best-fit model for the Mg XII line is based on jointly fitting the HEG and MEG data, though we show only the MEG data here.

width of $\sigma = 1200^{+200}_{-170}$ km s⁻¹. This shifted-Gaussian fit is statistically indistinguishable from the wind profile model fit. Although the *windprofile* fit is more meaningful, as it is based on a physically realistic model while having no more free parameters than the Gaussian model, the Gaussian fit confirms and quantifies the large line widths and blue shifts expected from EWS emission.

Along similar lines, He-like complexes can be fit with three Gaussians, providing a direct measure of the f/i ratio, from which a single radius of formation can be inferred. We show these results in Fig. 6. For the Mg XI complex we find a low ratio of $0.40^{+0.23}_{-0.17}$. We next fit the same model, but with the f/i ratio fixed at the “low density limit” that would be expected if the X-ray plasma were very far from the photosphere, where photoexcitation cannot alter the ratio. This fit (which is also shown in Fig. 6) is poor compared to the $f/i = 0.4$ fit, implying that the hot plasma is relatively close to the photosphere. This conclusion is in good agreement with the result from fitting the three wind-profile model (*hewind*), in which the onset radius of a distributed source of X-ray emitting plasma, R_o , is constrained to be within 1 stellar radius of the photosphere.

Porosity, due to optically thick clumps, can affect X-ray line profiles by reducing the average optical depth of the wind (Oskinova et al. 2006), and is another effect we might consider when fitting the emission line data. However, the porosity length that is necessary to provide a measurable effect is quite large (Owocki & Cohen 2006) compared to the small-scale structure in state-of-the-art 2-D radiation hydrodynamics simulations (Dessart & Owocki 2003, 2005). To explore the effects of porosity on the fit quality and on the other parameters, we fit the Mg XII Ly α line with a model having an effective opacity modified by porosity from spherical clumps. This model is similar to the one described in Owocki & Cohen (2006) – using the same porosity-length ($h(r) \equiv \ell/f$, where ℓ is the characteristic clump size and f is the clump filling factor) formalism – but here employing a radial clump distribution determined by the wind beta-velocity law, as used by Oskinova et al. (2006). We fix the characteristic optical depth at $\tau_* = 4.2$, which is the value we would expect at the wavelength of the Mg Ly α line assuming a mass-loss rate of $1.8 \times 10^{-5} M_{\odot} \text{ yr}^{-1}$ (Taresch et al. 1997). The fit we obtain is similar in quality to the *windpro-*

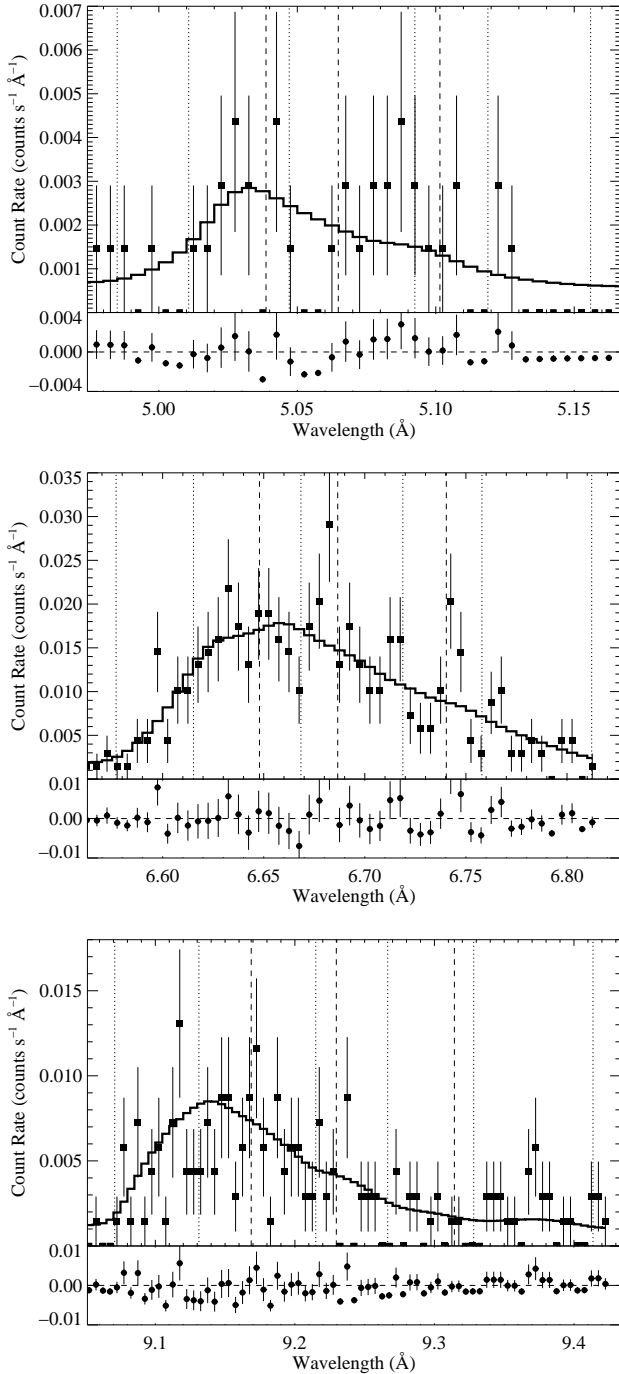


Figure 5. The MEG data for the helium-like line complexes: S XV (top), Si XIII (middle) and Mg XI (bottom). We show line center and terminal velocity indicators as in the previous figure, but here, we show three groups; one for each of the three lines in each complex. The best-fit models are based on jointly fitting the HEG and MEG data (except for the weaker S XV complex, where we fit only the MEG data). Note the very weak forbidden line in both the Mg and Si complexes (longest wavelength of the three lines in each complex).

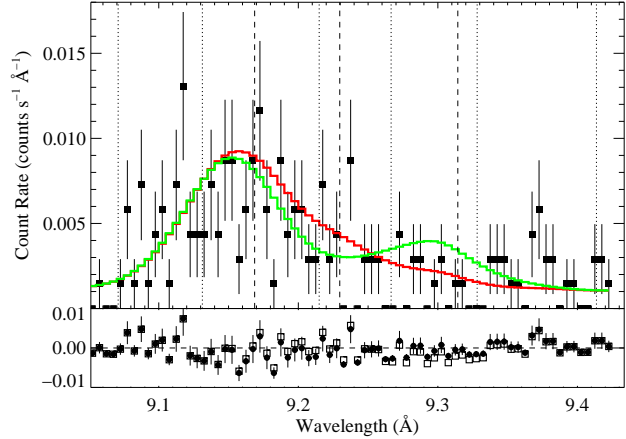


Figure 6. The MEG data for the Mg XI line complex fit with three shifted Gaussians. When the f/i ratio is a free parameter (red), it is low (0.4^{+23}_{-17}). When the ratio is fixed at the normal, equilibrium limit ($f/i = 2.7$) with no photoexcitation, as would be expected far from the star (green), the fit is poor.

file fit reported in Table 2. But in order to achieve this good fit, a very large terminal porosity length of $h_\infty = 5.3 R_*$ is required (with a 68% lower confidence limit of $h_\infty = 2.5 R_*$), where the radially varying porosity length is given by $h(r) = h_\infty(1 - R_*/r)^\beta$. If we use $2.6 \times 10^{-5} M_\odot \text{ yr}^{-1}$ as the standard, smooth-wind mass-loss rate (Repolust et al. 2004), then the required porosity length is even larger. Even the minimum porosity length of $h_\infty = 2.5 R_*$ is inconsistent with the numerical simulations of the line-driving instability (Dessart & Owocki 2003, 2005), requiring, for example, clumps that are individually $0.25 R_*$ in scale in a wind with a uniform filling factor of $f_v = 0.1$.

3.2 Mass-loss rate determination from the line profiles

Given the characteristic optical depth values (τ_* , listed in Table 2) obtained from fitting each line with the *windprofile* model, we can derive constraints on the wind mass-loss rate of HD 93129A. The characteristic optical depth is defined as $\tau_* \equiv \kappa \dot{M} / 4\pi R_* v_\infty$, so that by assuming a model of the bulk wind's X-ray opacity, $\kappa(\lambda)$, as well as a value for the stellar radius and wind terminal velocity, we can fit the wavelength-dependent τ_* values with the mass-loss rate as the only free parameter of the fit, as $\dot{M} = 4\pi R_* v_\infty \tau_*(\lambda) / \kappa(\lambda)$. We have demonstrated this process for analyzing the *Chandra* grating spectrum of the O supergiant ζ Pup (Cohen et al. 2010). Because of the lower quality of the *Chandra* spectrum of HD 93129A compared to that of ζ Pup, and because of the much smaller number (5 vs. 16) and narrower wavelength range of usable lines, the wavelength trend in τ_* is not apparent for HD 93129A. However, the five τ_* values are certainly consistent with the expected wavelength trend.

We constructed a model of the bulk wind opacity for HD 93129A, assuming that H and He are fully ionized, and assuming typical values for the ionization balance of metals (generally dominated by triply ionized states). Furthermore, we assume solar abundances from Asplund et al. (2009), except for C, N, and O, which are altered by CNO processing,

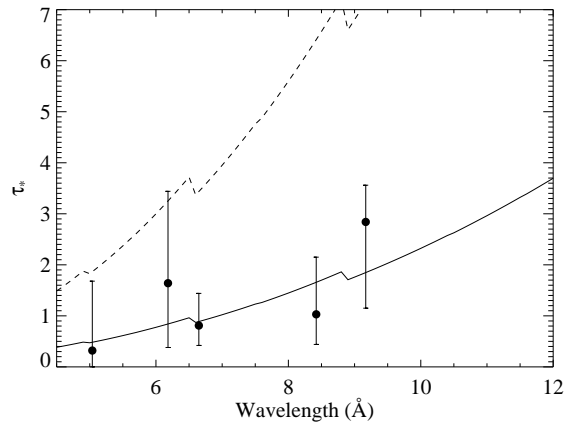


Figure 7. The five τ_* values fit with a single opacity model in order to derive \dot{M} . The best-fit τ_* model ($\dot{M} = 6.8 \times 10^{-6} M_{\odot} \text{ yr}^{-1}$) is shown as a solid line, while the dotted line represents that form of τ_* that would be expected if the traditional mass-loss rate of $2.6 \times 10^{-5} M_{\odot} \text{ yr}^{-1}$ (Repolust et al. 2004) were correct.

according to the spectral analysis of Taresch et al. (1997). We take the C, N, and O values from these authors, but rescale them so that the sum of the abundances of these three elements is equal to the sum of the C, N, and O in the Asplund et al. (2009) solar abundances. This effectively gives us $Z_{\text{C}} = 0.25$, $Z_{\text{N}} = 3.02$, and $Z_{\text{O}} = 0.47$, where Asplund et al. (2009) is the solar reference. We should note, however, that because the emission lines we derive τ_* values from are all at short wavelengths, the alterations to C, N, and O abundances have almost no effect on our results. Changing the overall metallicity – which we assume to be solar – would have an effect, however. The derived mass-loss rate scales inversely with the metallicity.

The result of fitting the τ_* values for the mass-loss rate is shown in Fig. 7. The best-fit mass-loss rate is $6.8_{-2.2}^{+2.8} \times 10^{-6} M_{\odot} \text{ yr}^{-1}$, using the stellar radius from Repolust et al. (2004). This represents a factor of three (Taresch et al. 1997) or four (Repolust et al. 2004) reduction with respect to traditional $\text{H}\alpha$ -based determinations that assume a smooth wind (and thus ignore optically thin clumping).

To check for consistency with the observed $\text{H}\alpha$, we modeled the profile with the line-blanketed, non-LTE, unified (photosphere+wind) model atmosphere code FASTWIND (Puls et al. 2005), which accounts for optically thin clumping (using the filling factor approach) in the calculations of the occupation numbers and the corresponding synthetic spectra. Stellar parameters were taken from Repolust et al. (2004), where the observational data also are described. However, we adopt the mass-loss rate derived from our X-ray analysis. We show the data in Fig. 8 along with three models, each with $\dot{M} = 7 \times 10^{-6} M_{\odot} \text{ yr}^{-1}$ and $\beta = 0.7$. The best model has a constant $f_v = 0.08$ above a radius $R_{cl} = 1.05 R_*$, below which the wind is assumed to be smooth. Note that this R_{cl} is not necessarily the same as the X-ray onset radius, R_o . In fact, this small clumping radius, R_{cl} is necessary to fit the data, as comparison with the model that assumes $R_{cl} = 1.3 R_*$ in Fig. 8 shows. In that model, the simulated strength of the core is much too low, reflecting the reduced $\text{H}\alpha$ opacity (which scales as \dot{M}^2/f_v) in the lower

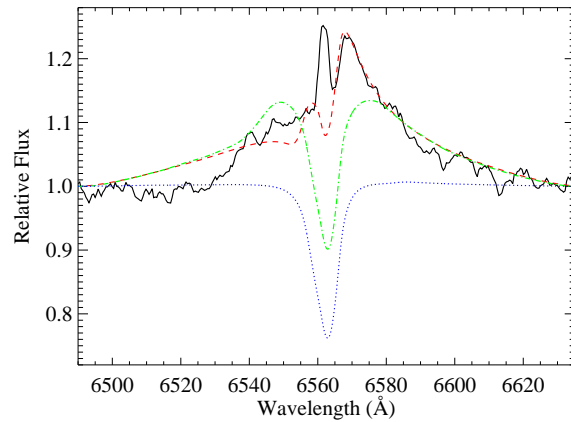


Figure 8. The $\text{H}\alpha$ emission profile (black, solid) is well reproduced by a model that includes clumping beginning at a radius of $R_{cl} = 1.05 R_*$ (red, dashed). The model with $R_{cl} = 1.3 R_*$ (green, dash-dot) does not have enough emission in the line core. For comparison, we show a model with no clumping (blue, dotted), in which the model fails to produce any emission. All models have $\dot{M} = 7 \times 10^{-6} M_{\odot} \text{ yr}^{-1}$ and $\beta = 0.7$. Note that the narrow emission peak at line center likely has a significant contribution from nebular emission, which we do not model.

wind. This early onset of wind clumping has been found for a number of other stars as well (Bouret et al. 2005; Puls et al. 2006). We also note that the simplest case of a spatially constant f_v actually reproduces the $\text{H}\alpha$ data reasonably well for this star, in contrast to, e.g., λ Cep, for which a rather strong radial dependence of f_v is needed (Sundqvist et al. 2011).

3.3 Global thermal modeling

While the individual line profiles provide information about the kinematics of the shock-heated plasma, its spatial distribution, and the degree of attenuation by the bulk wind in which the shock-heated plasma is embedded, complementary information is contained in the overall spectral energy distribution. The broadband spectrum provides information about the temperature distribution of the shock-heated plasma and also the wind mass-loss rate via the degree of attenuation of the X-rays. So, to complement the spectral modeling of individual emission lines, described in the previous two subsections, we fit global thermal models to the low-resolution zeroth-order spectrum of component A shown in Fig. 2.

The model assumes optically thin, collisional-radiative equilibrium (“coronal”) emission (*vapec*, the (Variable abundance) Astrophysical Plasma Emission Code (Smith et al. 2001)). It is attenuated by the cold, neutral interstellar medium (via the XSPEC model *tbabs* (Wilms et al. 2000)) and – for the EWS emission – the partially ionized stellar wind (via the XSPEC custom model *windtabs*³ (Leutenegger et al. 2010)). We model the EWS emission with a single isothermal *vapec* spectrum. To account for

³ This model is also described on the *windprofile* custom model page on the XSPEC site.

the contribution of harder X-rays from the wind-wind interaction we include a second thermal emission component⁴ attenuated only by the ISM.

This composite model is invoked in XSPEC as $(vapec \times windtabs + vapec) \times tbabs$. The free parameters of the model include the temperatures of the two *vapec* components, their emission measures, the characteristic mass column, $\Sigma_* \equiv \tau_*/\kappa$ (g cm^{-2}), of the wind absorption model, *windtabs*, and the interstellar column density. Fixed parameters include the metallicity (fixed at solar, except for CNO) of the emission model and the wind velocity profile (described by $\beta = 0.7$) of the wind attenuation model. We note that the *windtabs* model (Leutenegger et al. 2010) has two features that make it distinct from interstellar attenuation models and make it more appropriate for the modeling attenuation by a stellar wind with embedded shocks: (1) it incorporates atomic cross sections from partially ionized species (e.g. O IV rather than neutral O) and assumes that H and He are fully ionized; and (2) it uses an exact radiation transport model appropriate to an emitter spatially distributed within the absorbing medium. Leutenegger et al. (2010) show that the attenuation from this realistic wind transport model differs significantly from the exponential (“slab”) attenuation implemented in ISM absorption models (their figures 5 and 8). For the fitting we report on here, we use a solar abundance (Asplund et al. 2009) wind opacity model, but with altered C, N, and O abundances according to Taresch et al. (1997), just as we did for the analysis of the ensemble of τ_* values discussed in the previous subsection. The *vapec* emission model assumes the same abundances as the *windtabs* absorption model.

We fit the above-described composite thermal emission with wind-plus-ISM absorption model to the zeroth-order spectrum extracted from the seven coadded pointings. This low-resolution CCD spectrum has significantly better signal-to-noise than the dispersed grating spectra, but at a resolving power ($E/\Delta E$) of only a few tens. It extends to lower energies (0.5 keV) than the dispersed spectrum effectively does. The zeroth-order spectrum does not suffer from significant pile-up effects (unlike bare ACIS observations of the same star). We use χ^2 as the goodness of fit statistic and put confidence limits on the fitted model parameters using the $\Delta\chi^2$ formalism of Press et al. (2007).

We let the interstellar column density be a free parameter of the fit, and found a best-fit value of $N_{\text{H}} = 4.1 \times 10^{21} \text{ cm}^{-2}$, which is very close to the value implied by the color excess ($N_{\text{H}} = 3.7 \times 10^{21} \text{ cm}^{-2}$ (Gagné et al. 2011)). The 68 percent confidence limits for N_{H} (ISM) extend from $3.5 \times 10^{21} \text{ cm}^{-2}$ to $5.0 \times 10^{21} \text{ cm}^{-2}$. The best-fit model has emission component temperatures of $kT = 0.61 \pm .02 \text{ keV}$ and $kT = 3.31_{-0.99}^{+2.11} \text{ keV}$, where the hotter component has only 6 percent of the total emission measure. We conjecture that this hotter component represents a small amount of CWS X-ray emission, presumably associated with the non-thermal radio emission detected in the system (Benaglia et al. 2006). Its contribution is negligible below photon energies of 2.5

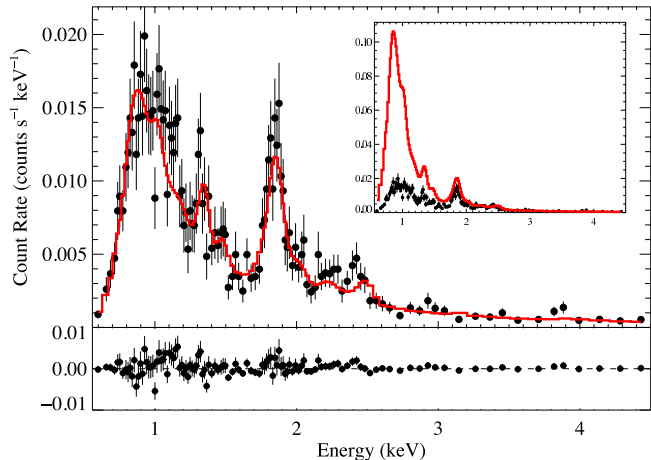


Figure 9. The same zeroth order ACIS CCD spectrum shown in Fig. 2, here fit with a two-temperature *apec* thermal emission model (red histogram), where one temperature component (0.6 keV) is attenuated by the stellar wind as well as the interstellar medium and the other (3.3 keV) is attenuated only by the ISM. Note the presence of strong Si XIII emission just below 2 keV. The vast majority of the emission in this spectrum is line emission, but due to the low resolution of the detector as well as the presence of many weak, blended lines, the spectrum looks relatively smooth. The inset figure shows the same data with a model identical to the best-fit model, except that the wind absorption (Σ_* in *windtabs*) is zeroed out. This model spectrum makes the significance of the wind absorption effect quite obvious. Nearly 80% of the emitted EWS X-rays are absorbed before they can escape from the wind.

keV. This provides further confirmation that the wind-wind X-rays do not affect the line profiles we discussed in the previous subsection.

The characteristic wind mass column density, Σ_* in the *windtabs* model, is found to be $\Sigma_* = 0.0522_{-0.0146}^{+0.0185} \text{ g cm}^{-2}$. Using the wind terminal velocity and stellar radius from Repolust et al. (2004), this corresponds to a mass-loss rate of $\dot{M} = 5.18_{-1.45}^{+1.83} \times 10^6 \text{ M}_{\odot} \text{ yr}^{-1}$. The biggest contribution to the uncertainty on the wind mass column density is the uncertainty on the interstellar absorption⁵. The quality of the fit is good, with a reduced χ^2 of 1.01 for 113 degrees of freedom. It is shown in Fig. 9.

We note the consistency of the broadband mass-loss rate determination with the independent determination from the ensemble of line profile shapes, discussed in the previous subsection. The wind attenuation is significant, as we show in Fig. 9, where we also include a model without wind attenuation. The X-ray luminosity (corrected for ISM attenuation) of the best-fit model is $L_{\text{X}} = 7.29 \times 10^{32} \text{ ergs s}^{-1}$ (giving $L_{\text{X}}/L_{\text{Bol}} = 1.3 \times 10^{-7}$), but when we also correct for wind attenuation, we find $L_{\text{X}} = 3.30 \times 10^{33} \text{ ergs s}^{-1}$. This implies that 78 percent of the X-ray emission above 0.5 keV produced by embedded wind shocks is absorbed before it escapes the wind (which can be seen graphically in the inset of Fig. 9). Note that nearly all of the X-ray emission below 0.5 keV will also be attenuated.

To further test the plasma emission temperature result,

⁴ Although the temperature distribution of the shocked plasma is certainly more complex than two discrete temperatures, we find that adding more temperature components does not improve the fit quality.

⁵ When we fix the ISM column density at $N_{\text{H}} = 2.5 \times 10^{21} \text{ cm}^{-2}$ (Taresch et al. 1997), the wind mass column density, and along with it, the mass-loss rate, increases by a factor of 1.8.

we can examine the temperature-sensitive iron L-shell line complexes in the 10 to 17 Å wavelength range of the grating spectrometer. The data do not have good signal-to-noise in that wavelength region and likely also suffer from modest contamination by dispersed photons from HD 93129B, as we discussed in §2. The contamination was primarily a concern with respect to the emission line shapes. But a contamination level of 20 or 25 % (based on Fig. 2) will not significantly skew the spectrum over a broad wavelength range. Because we want to ignore the contaminated line shapes, and to enhance the signal-to-noise ratio, we rebinned the MEG spectrum, using a 20 counts per bin criterion. We then fit the 10 to 16 Å portion⁶ of the MEG spectrum with an *apec* emission model, including wind attenuation via *windtabs* and interstellar absorption via *tbabs*. We fixed the wind mass column parameter of *windtabs* at the best-fit value found in our global fitting reported on earlier in this subsection and fixed the interstellar column density at $N_{\text{H}} = 3.7 \times 10^{21} \text{ cm}^{-2}$.

Because of the large number of charge states with closely spaced ionization energies, Fe L-shell emission is a sensitive diagnostic of plasma temperature (Behar et al. 2001). Ne-like Fe xvii, with strong emission lines near 15 and 17 Å, is present over a moderately wide range of temperatures, and dominates over higher charge states below about $kT = 0.3 \text{ keV}$. Fe xviii has strong lines near 14.2 and 16 Å and Fe xx has strong lines near 12.8 Å. Higher ionization states have strong lines primarily between 11 and 12 Å.

In Fig. 10 we show the binned MEG data along with the best-fit thermal emission model, which has a temperature of $kT = 0.58 \text{ keV}$, in very good agreement with the zeroth order spectral fitting. Here, though, we can see which specific lines are and are not contributing to the observed flux. The strong emission of Fe xvii is seen clearly near 15 Å, but there is no strong emission from the higher charge states. Thus, the dominant plasma temperature is constrained to be about 0.6 keV or lower, while only very small contributions from higher temperatures are compatible with the data.

3.4 HD 93129B

The zeroth order spectrum of HD 93129B, the O3.5 companion at a separation of $2.7''$, is shown in Fig. 2. We have also fit it with a thermal emission model with both wind and ISM absorption (but no CWS component), much as we did for HD 93129A. Because of the low signal-to-noise of this spectrum, we held the interstellar column density fixed at $N_{\text{H}} = 3.7 \times 10^{21} \text{ cm}^{-2}$, corresponding to the measured color excess. Our best-fit model has a temperature of $kT = 0.31 \pm .06 \text{ keV}$ and a wind absorption mass column of $\Sigma_* = 0.0221_{-0.0113}^{+0.0267} \text{ g cm}^{-2}$, corresponding to a mass-loss rate of $\dot{M} \approx 1 \times 10^{-6} M_{\odot} \text{ yr}^{-1}$, with a factor of two uncertainty.

We note that this source emission temperature is somewhat lower than that reported in Nazé et al. (2011). This is most likely due to our inclusion of wind absorption, which hardens the emergent spectrum. The ISM-corrected X-ray luminosity of our best-fit model is $L_{\text{X}} = 1.5 \times 10^{32} \text{ ergs s}^{-1}$,

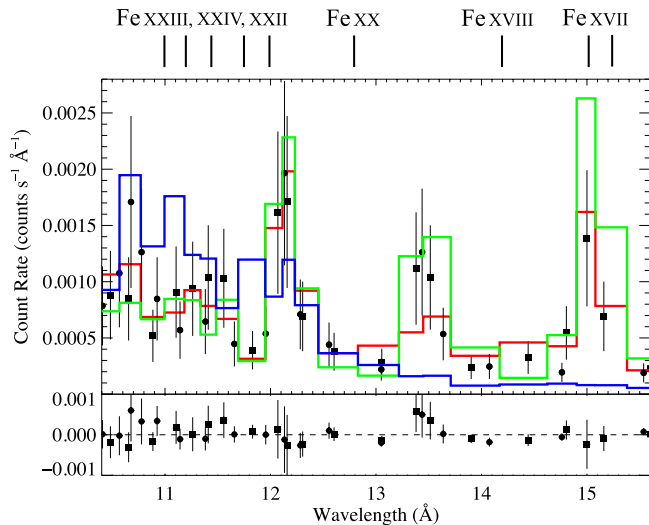


Figure 10. The binned MEG spectrum (squares are -1 order and circles +1 order) is shown along with the best-fit (MEG -1 order) model (red). Cooler (0.3 keV, green) and hotter (1.5 keV, blue) models are also shown, making it clear that the presence of Fe xvii emission near 15 Å in the data and the low levels of emission near 11 Å from higher ionization stages are incompatible with very hot ($kT > 1 \text{ keV}$) plasma from colliding wind shocks. Ne ix and x emission complexes are also visible at 13.5 Å and 12.1 Å, respectively. Their ratio is temperature dependent and consistent with temperatures between 0.3 and 0.6 keV. We indicate the wavelengths of some of the strongest lines at low and at high temperatures. Note that there are other, low-temperature lines of, e.g., Ne ix contributing to the observed flux in the short wavelength side of the spectral region displayed in this figure.

corresponding to $L_{\text{X}}/L_{\text{Bol}} = 1.2 \times 10^{-7}$, very similar to the value we find for component A.

4 DISCUSSION

The *Chandra* observations of HD 93129A are consistent with the embedded wind shock scenario that is generally assumed to apply to all O stars. The X-ray luminosity is $L_{\text{X}} = 1.3 \times 10^{-7} L_{\text{Bol}}$; very much in line with the canonical value for O star wind-shock sources (Pallavicini et al. 1981), although it is roughly a factor of two higher than the average value found for O stars in Carina (Nazé et al. 2011). The emission temperature is quite low (0.6 keV), as is expected from the EWS mechanism, although there is evidence for a small ($\sim 6\%$) contribution from hotter plasma (3.3 keV). The presence of this hotter component is not surprising, given the detection of non-thermal radio emission from the system, presumably associated with colliding wind shocks involving components Aa and Ab, separated by roughly 100 AU. But we stress that the colliding-wind contribution to the overall X-ray spectrum is minimal.

Although the EWS emission temperature of 0.6 keV is low, the overall spectrum is relatively hard. We have shown here, using both the individual line profiles and also the broadband, low-resolution CCD spectrum, that this is due to attenuation by the star’s dense stellar wind. The two different, largely independent, manifestations of the wind attenuation lead to consistent mass-loss rate determinations

⁶ Absorption renders the iron line complex near 17 Å undetected.

of between 4.7 and $7.0 \times 10^{-6} M_{\odot} \text{ yr}^{-1}$, which represent a factor of several reduction in the mass-loss rate over traditional values determined from density-squared diagnostics. As both X-ray mass-loss rate diagnostics are insensitive to density squared effects, and because some clumping is certainly expected in the wind of HD 93129A (Lépine & Moffat 2008), the new, lower mass-loss rate seems quite reasonable, and is in line with the factor of three mass-loss rate reduction seen in ζ Pup (Puls et al. 2006; Cohen et al. 2010). This is verified by our modeling of the H α line, which shows that $\dot{M} = 7 \times 10^{-6} M_{\odot} \text{ yr}^{-1}$ provides a good fit if a constant clump volume filling factor $f_v = 0.08$ is assumed. To explain the strong core of the H α line, a clump onset radius of $R_{cl} = 1.05 R_*$ also must be assumed. We note that the X-rays are not produced at radii this small. Presumably the wind shocks associated with clumps at the slow-moving base of the wind are not strong enough to produce X-rays.

The kinematics of the X-ray emitting plasma in HD 93129A determined from the line widths are consistent with the terminal velocity of the bulk wind ($v_{\infty} = 3200 \text{ km s}^{-1}$), assuming a constant X-ray filling factor above some onset radius, R_o . We derive R_o values for each line or line complex from the profile fitting, and find onset radii that are somewhat lower than, but still statistically consistent with, the typical value of $R_o \sim 1.5 R_*$ from numerical simulations of the line-driving instability (Owocki et al. 1988; Feldmeier et al. 1997; Runacres & Owocki 2002). However, if the wind terminal velocity is lower than we assumed for our fitting, then the R_o values would increase by 0.1 or 0.2, to $R_o \sim 1.5 R_*$ (for an assumed $v_{\infty} = 3000 \text{ km s}^{-1}$).

The location of the X-ray plasma is further constrained by the forbidden-to-intercombination line ratios in the helium-like line complexes observed in the grating spectra. Using a model that includes both the broadening and attenuation effects on the line profiles in conjunction with the altered forbidden-to-intercombination line ratios due to UV photoexcitation, we find that all three helium-like line complexes are completely consistent with the X-ray emitting plasma being distributed throughout the wind of HD 93129A, starting at a height of only several tenths of a stellar radius above the photosphere. Using a simpler model where we fit the forbidden-to-intercombination line ratio directly, using Gaussian profiles, we find low f/i ratios for the Si XIII and the Mg XI complexes. For both these complexes, the ratio expected if photoexcitation is unimportant, as would be the case in a binary wind-wind collision zone far from either star's photosphere, is ruled out with greater than 95% confidence.

Finally, we must discuss alternative interpretations of the spectra and, especially, the spectral lines. The profiles, while skewed and blue-shifted, are not as asymmetric as expected given the very high mass-loss rate traditionally found for the star. Our interpretation is that this is due to an actual mass-loss rate that is modestly lower than the traditional value, but in principle, it could also be due to porosity associated with optically thick and presumably large-scale wind clumping. However, not only are the required porosity lengths very high, but the same clumps that would need to be invoked to generate a porosity effect would also lead to a mass-loss rate reduction due to their effect on density-squared diagnostics. If, for example, the required porosity lengths were achieved with clumps having a size scale of 0.25

R_* and a uniform filling factor of $f_v = 0.1$ in the context of an H α mass-loss rate of $\dot{M} = 1.8 \times 10^{-5} M_{\odot} \text{ yr}^{-1}$ that assumes no clumping (Taresch et al. 1997), then the filling factor alone, via its effect on the density-squared mass-loss rate, would reduce the mass-loss rate inferred from the H α to a value consistent with what we find from the X-rays *without having to invoke any porosity* – as we have shown at the end of §3.2 and in Fig. 8. Any additional effect from porosity would make the mass-loss rates too low and the X-ray line profiles too symmetric.

5 CONCLUSIONS

We have shown that the *Chandra* grating spectrum of the extreme O star, HD 93129A, can be understood using the same paradigm that explains the canonical embedded wind shock source, ζ Pup, once adjustments are made for its larger wind terminal velocity and mass-loss rate. Specifically, the kinematics of the X-ray emitting plasma are consistent with shocks embedded in a $\beta = 0.7$, $v_{\infty} = 3200 \text{ km s}^{-1}$ wind starting at several tenths R_* , and that the attenuation signatures in the line profiles are consistent with a mass-loss rate of 4.7 to $7.0 \times 10^{-6} M_{\odot} \text{ yr}^{-1}$, representing a modest reduction compared to traditional mass-loss rates determined from H α measurements that ignore the effects of clumping, and showing consistency with H α modeling that includes modest clumping, in line with what is seen in LDI simulations (Dessart & Owocki 2005). This mass-loss rate reduction of a factor of three to four is consistent with that found for ζ Pup (Cohen et al. 2010). We have also demonstrated for the first time that modeling wind absorption of X-rays for both line profiles and for the broadband spectral energy distribution leads to consistent results when a physically realistic model of the broadband wind attenuation (Leutenegger et al. 2010) is used.

The global spectral modeling indicates that the dominant thermal emission component has quite a modest temperature, of roughly 0.6 keV, as predicted by EWS models. The observed overall hardness of the spectrum is attributable to wind attenuation, rather than high plasma temperatures. The low dominant plasma temperature is also manifest in the low Si XIV/Si XIII ratio, which is consistent with the value found in the *Chandra* grating spectrum of ζ Pup. There is likely a small amount of hard X-ray emission from colliding wind binary interaction between components Aa and Ab, many tens of AU from either star's photosphere. Because of the large separation of the components, this X-ray emission makes a small contribution to the overall X-ray spectral properties, representing less than 10% of the system's X-ray luminosity. The helium-like f/i ratios also provide evidence that the bulk of the X-rays arise in embedded wind shocks.

As HD 93129A is the earliest O star known, and has one of the strongest winds of any O star, the work presented here strongly suggests that the embedded wind shock scenario, as described by numerical simulations of the line-driving instability, is widely applicable to O stars, even those with extremely strong winds. And that X-ray line profile analysis, especially in conjunction with broadband spectral modeling, provides a good means of making a clumping-independent mass-loss rate determination for O stars with dense winds.

ACKNOWLEDGMENTS

Support for this work was provided by the National Aeronautics and Space Administration through *Chandra* award numbers AR7-8002X and GO0-11002B to Swarthmore College. EEW was supported by a Lotte Lazarsfeld Bailyn Summer Research Fellowship and JPM was supported by a Surdna Summer Research Fellowship, both from the Provost's Office at Swarthmore College. MAL is supported by an appointment to the NASA Postdoctoral Program at Goddard Space Flight Center, administered by Oak Ridge Associated Universities through a contract with NASA. JOS and SPO acknowledge support from NASA award ATP NNX11AC40G to the University of Delaware. The authors thank Véronique Petit for her careful reading of the manuscript and several useful suggestions.

REFERENCES

- Antokhin I. I., Owocki S. P., Brown J. C., 2004, *ApJ*, 611, 434
- Asplund M., Grevesse N., Sauval A. J., Scott P., 2009, *ARAA*, 47, 481
- Babel J., Montmerle T., 1997, *ApJ*, 485, L29
- Behar E., Cottam J., Kahn S. M., 2001, *ApJ*, 548, 966
- Benaglia P., Koribalski B., 2004, *A&A*, 416, 171
- Benaglia P., Koribalski B., Albecete Colombo J. F., 2006, *PASA*, 23, 50
- Bouret J. C., Lanz T., Hillier D. J., 2005, *A&A*, 438, 301
- Canizares C. R., et al., 2005, *PASP*, 117, 1144
- Cash W., 1979, *ApJ*, 228, 939
- Cassinelli J. P., Miller N. A., Waldron W. L., MacFarlane J. J., Cohen D. H., 2001, *ApJ*, 554, L55
- Cohen D. H., Leutenegger M. A., Wollman E. E., Zsargó J., Hillier D. J., Townsend R. H. D., Owocki S. P., 2010, *MNRAS*, 405, 2391
- Dere K. P., Landi E., Young P. R., Del Zanna G., Landini M., Mason H. E., 2007, *A&A*, 498, 915
- Dessart L., Owocki S. P., 2003, *A&A*, 406, L1
- Dessart L., Owocki S. P., 2005, *A&A*, 437, 657
- Evans N. R., Seward F. D., Krauss M. I., Isobe T., Nichols J., Schlegel E. M., Wolk S. J., 2003, *ApJ*, 589, 509
- Feldmeier A., Puls J., Pauldrach A. W. A., 1997, *A&A*, 322, 878
- Gagné M., et al., 2011, *ApJS*, in press (arXiv:1103.1149)
- Gagné M., Oksala M., Cohen D. H., Tonnesen S. K., ud-Doula A., Owocki S. P., Townsend R. H. D., MacFarlane J. J., 2005, *ApJ*, 628, 986
- Hamann W.-R., Feldmeier A., Oskinova L. M., 2008, *Clumping in Hot Star Winds*. Universitätsverlag, Potsdam
- Kahn S. M., Leutenegger M. A., Cottam J., Rauw G., Vreux J.-M., den Boggende A. J. F., Mewe R., Güdel M., 2001, *A&A*, 365, L312
- Lanz T., Hubeny I., 2003, *ApJS*, 146, 417
- Lépine S., Moffat A. F. J., 2008, *AJ*, 136, 548
- Leutenegger M. A., Paerels F. B. S., Kahn S. M., Cohen D. H., 2006, *ApJ*, 650, 1096
- Leutenegger M. A., Cohen D. H., Zsargó J., Martell E. M., MacArthur J. P., Owocki S. P., Gagné M., Hillier D. J., 2010, *ApJ*, 719, 1767
- Lucy L. B., White R. L., 1980, *ApJ*, 241, 300
- Nazé Y., et al., 2011, *ApJS*, in press (arXiv:1103.0101)
- Nelan E. P., Walborn N. R., Wallace D. J., Moffat A. F. J., Makidon R. B., Gies D. R., Panagia N., 2004, *AJ*, 128, 323
- Nelan E. P., Walborn N. R., Wallace D. J., Moffat A. F. J., Makidon R. B., Gies D. R., Panagia N., 2010, *AJ*, 139, 2714
- Nichols J., Mitschang A. W., Waldron W., Walborn N., 2011, *ApJ*, in preparation
- Oskinova L., Feldmeier A., Hamann W.-R., 2006, *MNRAS*, 372, 313
- Owocki S. P., Castor J. I., Rybicki G. B., 1988, *ApJ*, 335, 914
- Owocki S. P., Cohen D. H., 2001, *ApJ*, 559, 1108
- Owocki S. P., Cohen D. H., 2006, *ApJ*, 648, 565
- Pallavicini R., Golub L., Rosner R., Vaiana G. S., Ayres T., Linsky J. L., 1981, *ApJ*, 248, 279
- Pittard J. M., Parkin E. R., 2010, *MNRAS*, 403, 1657
- Press W. H., Flannery B. P., Teukolsky S. A., Vetterling W. T., 2007, *Numerical Recipes*, 3rd edition. Cambridge University Press, Cambridge
- Puls J., Markova N., Scuderi S., Stanghellini C., Taranova O. G., Burnley A. W., Howarth I. D., 2006, *A&A*, 454, 625
- Puls J., Urbaneja M. A., Venero R., Repolust T., Springmann U., Jokuthy A., Mokiem M. R., 2005, *A&A*, 435, 669
- Repolust T., Puls J., Herrero A., 2004, *A&A*, 415, 349
- Runacres M. C., Owocki S.P., 2002, *A&A*, 381, 1015
- Smith R. K., Brickhouse N. S., Liedahl D. A., Raymond J. C., 2001, *ApJ*, 556, L91
- Stevens I. R., Blondin J. M., Pollock A. M. T., 1992, *ApJ*, 386, 265
- Sundqvist J. O., Puls J., Feldmeier A., Owocki S. P., 2011, *A&A*, 528, 64
- Townsley L., et al., 2011, *ApJS*, (arXiv:1102.4779)
- Taresch G., et al., 1997, *A&A*, 321, 531
- ud-Doula A., Owocki S.P., 2002, *ApJ*, 576, 413
- Walborn N. R., 2008, *Rev. Mex.*, 33, 5
- Walborn N. R., et al., 2002, *AJ*, 123, 2754
- Walborn N. R., Nichols J. S., Waldron W. L., 2009, *ApJ*, 703, 633
- Westbrook O. W., et al., 2008, *ApJS*, 176, 218
- Wilms J., Allen A., McCray R., 2000, *ApJ*, 542, 914